

# ***XRISM* forecast for the Coma cluster: stormy, with a steep power spectrum**

XRISM COLLABORATION:

MARC AUDARD, HISAMITSU AWAKI, RALF BALLHAUSEN, AYA BAMBA, EHUD BEHAR, ROZENN BOISSAY-MALAUQUIN, LAURA BRENNEMAN, GREGORY V. BROWN, LIA CORRALES, ELISA COSTANTINI, RENATA CUMBEE, MARIA DIAZ TRIGO, CHRIS DONE, TADAYASU DOTANI, KEN EBISAWA, MEGAN E. ECKART, DOMINIQUE ECKERT, SATOSHI EGUCHI, TERUAKI ENOTO, YUICHIRO EZOE, ADAM FOSTER, RYUICHI FUJIMOTO, YUTAKA FUJITA, YASUSHI FUKAZAWA, KOTARO FUKUSHIMA, AKIHIRO FURUZAWA, LUIGI GALLO, JAVIER A. GARCÍA, LIYI GU, MATTEO GUAINAZZI, KOUICHI HAGINO, KENJI HAMAGUCHI, ISAMU HATSUKADE, KATSUHIRO HAYASHI, TAKAYUKI HAYASHI, NATALIE HELL, EDMUND HODGES-KLUCK, ANN HORNSCHEMEIER, YUTO ICHINOHE, DAIKI ISHI, MANABU ISHIDA, KUMI ISHIKAWA, YOSHITAKA ISHISAKI, JELLE KAASTRA, TIMOTHY KALLMAN, ERIN KARA, SATORU KATSUDA, YOSHIAKI KANEMARU, RICHARD KELLEY, CAROLINE KILBOURNE, SHUNJI KITAMOTO, SHOGO KOBAYASHI, TAKAYOSHI KOHMURA, AYA KUBOTA, MAURICE LEUTENEGGER, MICHAEL LOEWENSTEIN, YOSHITOMO MAEDA, MAXIM MARKEVITCH, HIRONORI MATSUMOTO, KYOKO MATSUSHITA, DAN MCCAMMON, BRIAN MCNAMARA, FRANÇOIS MERNIER, ERIC D. MILLER, JON M. MILLER, IKUYUKI MITSUISHI, MISAKI MIZUMOTO, TSUNEFUMI MIZUNO, KOJI MORI, KOJI MUKAI, HIROSHI MURAKAMI, RICHARD MUSHOTZKY, HIROSHI NAKAJIMA, KAZUHIRO NAKAZAWA, JAN-UWE NESS, KUMIKO NOBUKAWA, MASAYOSHI NOBUKAWA, HIROFUMI NODA, HIROKAZU ODAKA, SHOJI OGAWA, ANNA OGORZALEK, TAKASHI OKAJIMA, NAOMI OTA, STEPHANE PALTANI, ROBERT PETRE, PAUL PLUCINSKY, FREDERICK S. PORTER, KATJA POTTSCHMIDT, KOSUKE SATO, TOSHIKI SATO, MAKOTO SAWADA, HIROMI SETA, MEGUMI SHIDATSU, AURORA SIMIONESCU, RANDALL SMITH, HIROMASA SUZUKI, ANDREW SZYMKOWIAK, HIROMITSU TAKAHASHI, MAI TAKEO, TORU TAMAGAWA, KEISUKE TAMURA, TAKAAKI TANAKA, ATSUSHI TANIMOTO, MAKOTO TASHIRO, YUKIKATSU TERADA, YUICHI TERASHIMA, YOHKO TSUBOI, MASAHIRO TSUJIMOTO, HIROSHI TSUNEMI, TAKESHI TSURU, AYŞEGÜL TÜMER, HIROYUKI UCHIDA, NAGOMI UCHIDA, YUUSUKE UCHIDA, HIDEKI UCHIYAMA, SHUTARO UEDA, YOSHIHIRO UEDA, SHINICHIRO UNO, JACCO VINK, SHIN WATANABE, BRIAN J. WILLIAMS, SATOSHI YAMADA, SHINYA YAMADA, HIROYA YAMAGUCHI, KAZUTAKA YAMAOKA, NORIKO YAMASAKI, MAKOTO YAMAUCHI, SHIGEO YAMAUCHI, TAHIR YAQOUB, TOMOKAGE YONEYAMA, TESSEI YOSHIDA, MIHOKO YUKITA, IRINA ZHURAVLEVA, ANDREW FABIAN, DYLAN NELSON, NOBUHIRO OKABE, ANNALISA PILLEPICH, CICELY POTTER, MANON REGAMEY, KOSEI SAKAI, MONA SHISHIDO, NHUT TRUONG, DANIEL R. WIK AND JOHN ZUHONE

## ABSTRACT

The *XRISM* Resolve microcalorimeter array measured the velocities of hot intracluster gas at two positions in the Coma galaxy cluster:  $3' \times 3'$  squares at the center and at  $6'$  (170 kpc) to the south. We find the line-of-sight velocity dispersions in those regions to be  $\sigma_z = 208 \pm 12$  km s<sup>-1</sup> and  $202 \pm 24$  km s<sup>-1</sup>, respectively. The central value corresponds to a 3D Mach number of  $M = 0.24 \pm 0.015$  and the ratio of the kinetic pressure of small-scale motions to thermal pressure in the intracluster plasma of only  $3.1 \pm 0.4\%$ , at the lower end of predictions from cosmological simulations for merging clusters like Coma, and similar to that observed in the cool core of the relaxed cluster A2029. Meanwhile, the gas in both regions exhibits high line-of-sight velocity differences from the mean velocity of the cluster galaxies,  $\Delta v_z = 450 \pm 15$  km s<sup>-1</sup> and  $730 \pm 30$  km s<sup>-1</sup>, respectively. A small contribution from an additional gas velocity component, consistent with the cluster optical mean, is detected along a sightline near the cluster center. The combination of the observed velocity dispersions and bulk velocities is not described by a Kolmogorov velocity power spectrum of steady-state turbulence; instead, the data imply a much steeper effective slope (i.e., relatively more power at larger linear scales). This may indicate either a very large dissipation scale resulting in the suppression of small-scale motions, or a transient dynamic state of the cluster, where large-scale gas flows generated by an ongoing merger have not yet cascaded down to small scales.

*Keywords:* Galaxy clusters (584) — Coma cluster (270) — Intracluster medium (858) — High resolution spectroscopy (2096)

## 1. INTRODUCTION

The weather in galaxy clusters is forecast to be stormy (Burns 1998). X-ray images and temperature maps of the hot intracluster medium (ICM) have long suggested that clusters

are dynamic objects — they show infalling subclusters undergoing ram pressure stripping and accompanied by shock fronts, as well as sharp “cold fronts” (e.g., Jones & Forman 1999; Briel & Henry 1994; Markevitch & Vikhlinin 2007). The cluster cores often exhibit buoyant AGN bubbles (e.g., Churazov et al. 2000; Fabian et al. 2006; McNamara & Nulsen 2007). Cluster radio images frequently show radio

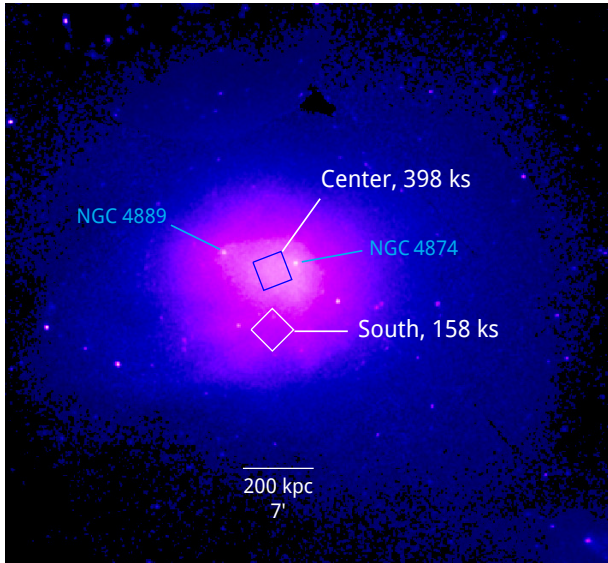


**Figure 1.** *XRISM* Resolve fields of view and exposure times overlaid on the *XMM-Newton* image of the Coma cluster (Sanders et al. 2020). The two brightest cluster galaxies are marked.

galaxies with bent and contorted tails, believed to trace the ICM winds (e.g., Burns 1998; Botteon et al. 2020).

The recently launched X-ray microcalorimeter array Resolve onboard the *XRISM* observatory (Tashiro et al. 2020; Ishisaki et al. 2022) picks up where its short-lived twin, *Hitomi* SXS (Takahashi et al. 2016; Kelley et al. 2016), left off. These instruments provide the first precise, *direct* look at gas velocities in galaxy clusters across various dynamical states. A microcalorimeter enables nondispersive high-resolution X-ray spectroscopy (by recording the energy of each incident photon independently of its source’s position in the sky), allowing us to map plasma velocities in clusters and other extended X-ray sources, such as supernova remnants, by measuring the Doppler line shifts and broadening of the plasma emission lines.

The line-of-sight (LOS) velocities and velocity dispersions have already been reported for the cool cores of the Perseus (Hitomi Collab. 2016), Centaurus (*XRISM* Collab. 2025b), and A2029 (*XRISM* Collab. 2025a) clusters. The dispersions are found to be in the  $\sigma_z \sim 120\text{--}190\text{ km s}^{-1}$  range<sup>1</sup>, which constrains the mechanical energy output of the cluster’s central AGN and its contribution to the thermal balance of the cores. The LOS velocities exhibit significant gradients across the cool cores in Perseus and Centaurus, revealing gas sloshing likely triggered by past cluster mergers.

In this Letter, we present the first Resolve measurements for a disturbed cluster without a cool core or a central powerful AGN — the nearby ( $z = 0.02333$ , Bilton & Pimblet 2018) Coma cluster. The cluster core has two dominant galaxies (BCG), NGC 4874 and NGC 4889, with LOS veloc-

ities differing by  $720\text{ km s}^{-1}$  (e.g., Colless & Dunn 1996). Both galaxies host small-scale X-ray coronae of  $T = 1\text{--}2\text{ keV}$  gas with  $r \sim 3\text{ kpc}$  — likely remnants of past cool cores stripped by ram pressure during a merger — surviving within the hot  $T = 8\text{--}9\text{ keV}$  ICM (Vikhlinin et al. 2001; Sanders et al. 2014). The galaxies also mark larger-scale bumps in the hot ICM density (Vikhlinin et al. 1997; Andrade-Santos et al. 2013), indicating underlying concentrations of dark mass, which are indeed seen in the weak-lensing mass map (Okabe et al. 2014).

On larger scales, the lensing map reveals distinct subhalos (Okabe et al. 2014). The ICM exhibits filamentary structures (Vikhlinin et al. 1997; Sanders et al. 2013), possibly resulting from stripping of merging subclusters. A prominent shock front  $\sim 1\text{ Mpc}$  west of center is propagating in the sky plane, as well as a contact discontinuity at a similar distance to the east (Planck Collab. 2013; Churazov et al. 2021), and a subgroup  $1.3\text{ Mpc}$  to the southwest (outside the main X-ray cluster body) is apparently on a return trajectory after passing through the main cluster (Churazov et al. 2021). All of the above indicates the presence of merging activity in the plane of the sky.

Coma hosts a cluster-wide giant radio halo (Brown & Rudnick 2011) — the synchrotron emission from ultrarelativistic electrons spinning in the magnetic field permeating the ICM. These electrons are believed to be continuously energized by turbulence in the ICM, though the efficiency of this mechanism is uncertain (Brunetti & Jones 2014). Along with random velocities, turbulence in the ICM should produce fluctuations in plasma density and pressure, which have indeed been observed in Coma using X-ray surface brightness and temperature maps (Schuecker et al. 2004; Churazov et al. 2012; Zhuravleva et al. 2019; Sanders et al. 2020).

With relatively flat gas density and temperature profiles in the central region (e.g., Arnaud et al. 2001; Sanders et al. 2020) and thus no steep radial entropy gradients (such as those present in cluster cool cores), as well as absence of AGN injecting bubbles into the ICM, Coma offers perhaps the simplest experimental setup among galaxy clusters to study ICM turbulence. It should be driven solely by structure formation and develop in a simple, isotropic manner, free of the complications of a stratified atmosphere. The goal of this work is to probe turbulence in the Coma core using the first precise measurements of ICM velocities.

We use  $H_0 = 70\text{ km s}^{-1}\text{ Mpc}^{-1}$ ,  $\Omega_m = 0.3$  flat cosmology, in which  $1' = 28.2\text{ kpc}$  at the cluster redshift. The uncertainties are 68%.

## 2. DATA

### 2.1. Observations

*XRISM* observed Coma during 2024 July 9-18 (obsid 300073010) with an aimpoint at  $\alpha = 194.944^\circ$ ,  $\delta = 27.947^\circ$  near the cluster’s X-ray center, referred to as “Center”, and during 2024 May 20-24 (obsids 300074010 and 300074020), with an aimpoint at  $\alpha = 194.941^\circ$ ,  $\delta = 27.847^\circ$ ,  $6'$  south of the center, referred to as “South”. In this paper, we utilize data from the Resolve instrument — a microcalorimeter ar-

<sup>1</sup> Hereafter the index  $z$  denotes the LOS component of the velocity.

**Table 1.** Parameters for one-component fits to spectra in full Center and South regions

	Center		South	
	2–9 keV	6.4–6.9 keV	2–9 keV	6.4–6.9 keV
$T$ , keV .....	$8.37 \pm 0.15$	$8.55 \pm 0.25$	$7.53 \pm 0.25$	$7.44 \pm 0.44$
Fe abundance .....	$0.32 \pm 0.01$	$0.33 \pm 0.02$	$0.36 \pm 0.025$	$0.32 \pm 0.04$
$z$ .....	$0.02183 \pm 0.00005$		$0.02089 \pm 0.00009$	
$\sigma_z$ , km s <sup>-1</sup> .....	$208 \pm 12$		$202 \pm 24$	

ray that covers a  $3.1' \times 3.1'$  area of the sky with  $6 \times 6$  pixels (except for one corner pixel illuminated by an internal calibration source), each producing a spectrum of incident X-rays with a resolution of 4.5 eV FWHM (Porter et al. 2024). The two Resolve pointings are overlaid on an *XMM-Newton* image of the cluster in Fig. 1.

The instrument’s energy band spans  $E = 1.7–12$  keV (limited at low energies by the attenuation of the window in the dewar gate valve that is currently closed) and includes the Fe XXV-XXVI emission line complex at  $E = 6.7–6.9$  keV (rest-frame), a dominant feature in the spectrum of the hot, optically-thin ICM.

## 2.2. Data Reduction

We extract spectra from the Resolve photon lists produced by the *XRISM* pipeline (Build 8, CalDB version 8 (20240315)), following the procedure detailed in *XRISM Collab. (2025a)*. We use only the high-resolution primary events. The Resolve pixel 27, which exhibits poorly modeled gain excursions, is excluded from the spectra, along with calibration pixel 12. The standard screening yields clean exposures of 398 ks for the Center and 158 ks for the South (where we co-add the two coaligned partial exposures of 85 ks and 73 ks). The heliocentric velocity corrections, accounting for the Earth’s velocity component toward the target, are  $-23.5$  km s<sup>-1</sup> (Center) and  $-21.6$  km s<sup>-1</sup> (South); all velocities and redshifts below are given in the heliocentric frame. We use the spectral redistribution matrix (RMF) of “L” size<sup>2</sup> for the results below; no significant changes to the results were found between “M”, “L” or “X” size matrices (which differ in the tradeoff between accuracy of modeling of secondary response components and convolution speed).

The Resolve energy scale (gain) is continuously calibrated in orbit, resulting in an energy scale uncertainty of  $\leq 0.3$  eV (field averaged) for the 5.4–9 keV band (Eckart et al. 2024; Porter et al. 2024; Eckart et al. 2025), corresponding to  $\leq 15$  km s<sup>-1</sup> Doppler shift instrumental uncertainty for a line at 6 keV.

The Resolve charged-particle induced non-X-ray background (NXB) is negligible for deriving the shapes of the cluster Fe lines, but it reaches about 10% of the continuum

signal from the Coma core at both ends of the useful band (at  $E \sim 2$  keV and 9 keV), so it needs to be accounted for when modeling the continuum. The cosmic X-ray background (CXB) is  $\lesssim 1\%$  of the cluster signal anywhere in this band. Therefore, for the spectral fits below, we included the NXB spectral model (continuum plus several emission lines) fit to the Resolve blank-sky data as described in *XRISM Collab. (2025b)*, but disregarded CXB for simplicity.

The angular resolution of the X-ray mirror is  $1.3'$  (half-power diameter, HPD, of the point-spread function, PSF). For spectra extracted from the full  $3'$  Resolve field of view (FOV), intermixing of photons from adjacent regions in the sky is relatively minor, especially for a cluster like Coma with a non-peaked X-ray brightness distribution. However, in spectra extracted from  $1.5'$  quadrants, about 50% of the recorded photons are scattered from adjacent regions. For qualitative purposes of §3.1–§4.3, we use spectral fits derived by disregarding PSF scattering (fitting spectra from adjacent regions independently of each other and using ancillary response functions, ARF, generated for point sources<sup>2</sup>), so those values are approximate. We do include PSF mixing in the forward modeling of the velocity differences in §4.3, where it has a significant effect, ensuring our results for the velocity power spectrum are precise.

## 3. RESULTS

### 3.1. Gas temperatures and abundances

Because Coma lacks a cluster-scale cool core and its projected temperature across the core is relatively uniform (e.g., Arnaud et al. 2001; Sanders et al. 2020), we expect the gas within each of our pointings to be well described by a single-temperature model. We therefore fit the Resolve spectra from the entire Center and South FOV (using the XSPEC package, Arnaud 1996) with a one-component thermal plasma emission model that includes thermal broadening (BAPEC, Smith et al. 2001), abundances relative to solar from Asplund et al. (2009), fixing Galactic absorption at  $N_H = 9.2 \times 10^{19}$  cm<sup>-2</sup> (which is unimportant for our energy band), and using a broad 2–9 keV band along with a narrow 6.4–6.9 keV interval that encompasses the Fe XXV-XXVI complex. The spectra for both regions are well-fitted, free of any systematic residuals; the fit parameters are provided in Table 1. Importantly, we find that the broad-band temperatures, primarily determined by the continuum slope, and the narrow-band temperatures,

<sup>2</sup> heasarc.gsfc.nasa.gov/docs/xrism/analysis/abc\_guide/xrism\_abc.html

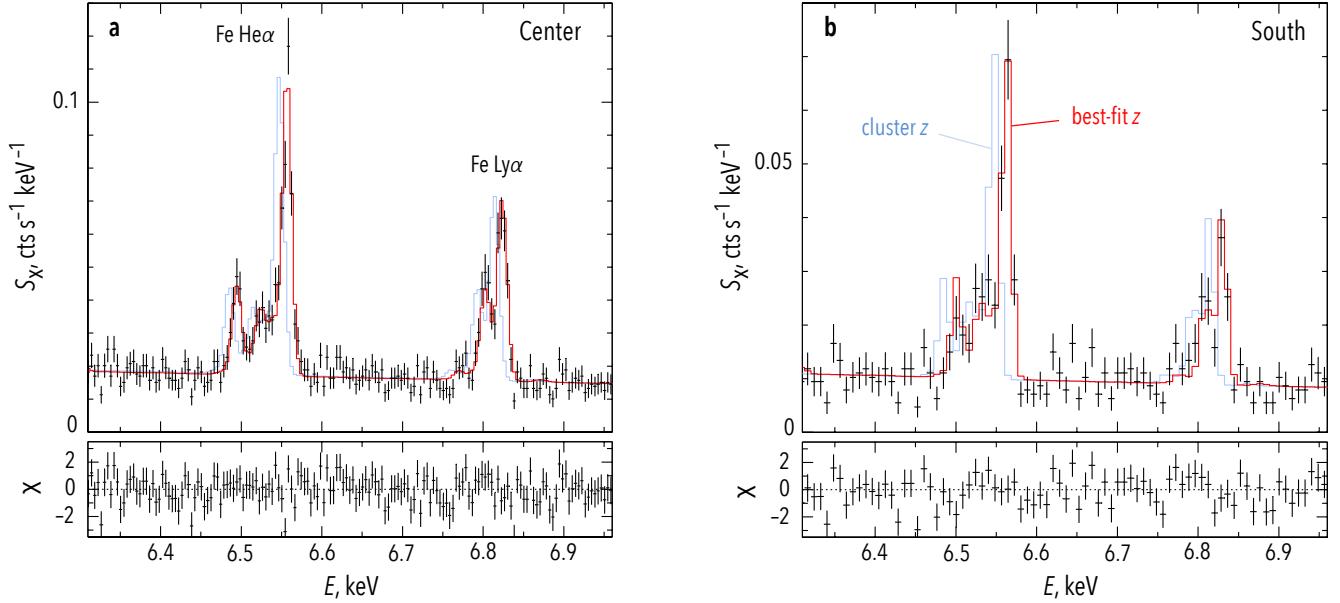


**Figure 2.** XRISM Resolve spectra for (a) Center and (b) South pointings in the He-like and H-like Fe line region, binned by 4 eV and 8 eV, respectively. Red lines show the best-fit models (Table 1), while the light blue line represents a model with the cluster optical redshift; a shift is evident.

primarily determined by the Fe XXVI/XXV flux ratio, are in good agreement within their tight errors. This gives confidence in the accuracy of the temperatures and the gas velocity dispersions (below), whose effect on the Fe line width combines (in quadrature) with the thermal broadening ( $\sigma_{\text{th},z} = 120 \text{ km s}^{-1}$  and  $112 \text{ km s}^{-1}$  for the Center and South temperatures, respectively). These temperatures will be compared with those from other X-ray instruments in a forthcoming paper. Based on these temperatures, the estimated sound speeds are  $c_s = (\gamma kT / \mu m_p)^{1/2} = 1508 \text{ km s}^{-1}$  and  $1407 \text{ km s}^{-1}$  for the Center and South regions, respectively (where  $\gamma = 5/3$  is the polytropic index and  $\mu = 0.6$  is the mean molecular weight of the intracluster plasma).

We also fit the Center spectrum with a model with independent abundances (BVAPEC). In addition to Fe, other elements with notable abundance constraints include Ni ( $0.43 \pm 0.11$ ), S ( $0.27 \pm 0.12$ ) and Ar ( $0.49 \pm 0.21$ ); others are detected at  $< 2\sigma$  significance.

### 3.2. Gas velocities and dispersions

The spectra of the Fe complex are shown in Fig. 2. The best-fit redshifts and LOS velocity dispersions  $\sigma_z$  with their statistical uncertainties are presented in Table 1. The lines in both regions (a) are narrow, with  $\sigma_z \approx 200 \text{ km s}^{-1}$ , and (b) show large velocity offsets from the cluster optical redshift ( $cz = 6995 \pm 39 \text{ km s}^{-1}$ , [Bilton & Pimblet 2018](#)),  $\Delta cz = -450 \pm 15 \text{ km s}^{-1}$  for the Center and  $-730 \pm 30 \text{ km s}^{-1}$  for the South. These offsets are evident in Fig. 2; they correspond to line shifts of 10 eV and 16 eV, much greater than the gain calibration uncertainty of 0.3 eV (§2). Both velocity offsets align with those derived in larger regions with *XMM-Newton*

([Sanders et al. 2020](#)), within the latter’s 10–20 times larger uncertainties.

The Center spectrum has approximately 940 and 510 counts in the FeXXV and XXVI complexes, respectively, which is sufficient for deriving velocities and dispersions in separate quadrants with good statistical precision. In contrast, the South spectrum has a total of 480 line counts. Results for the quadrants in the Center pointing, along with their typical uncertainties, are shown in Fig. 3 (except for dispersions in the South, which have large uncertainties). There are significant variations in line width within the Center; the SE quadrant shows a narrower line than the field average, while the NW quadrant exhibits a broader line.

The Fe XXV He- $\alpha$  complex for the NW quadrant is shown in Fig. 4; the line shape suggests the presence of at least one additional component at an energy below the main peak. Allowing for two plasma components with free  $z$  and  $kT$  and the same (free) velocity dispersion and chemical abundances, improves the fit by  $\Delta\chi^2 = 10.6$  for 3 additional parameters. This component contributes  $22 \pm 7\%$  of the total emission measure, with a best-fit  $z = 0.0233 \pm 0.0004$  consistent with the cluster’s optical redshift, while the main component deviates from it by  $\Delta cz = -470 \text{ km s}^{-1}$ . Their best-fit dispersion is  $127 \pm 41 \text{ km s}^{-1}$ , with temperatures of  $9.4 \pm 0.8 \text{ keV}$  and  $6.8 \pm 1.8 \text{ keV}$  for the main and additional components, respectively. While temperatures of the two components are statistically indistinguishable, the relatively high temperature for the additional component does suggest that the gas is located in the cluster core (rather than being projected from the cooler outskirts) — possibly related to the X-ray brightness excess associated with NGC 4874 ([Vikhlinin et al. 1997](#); [Andrade-Santos et al. 2013](#)).

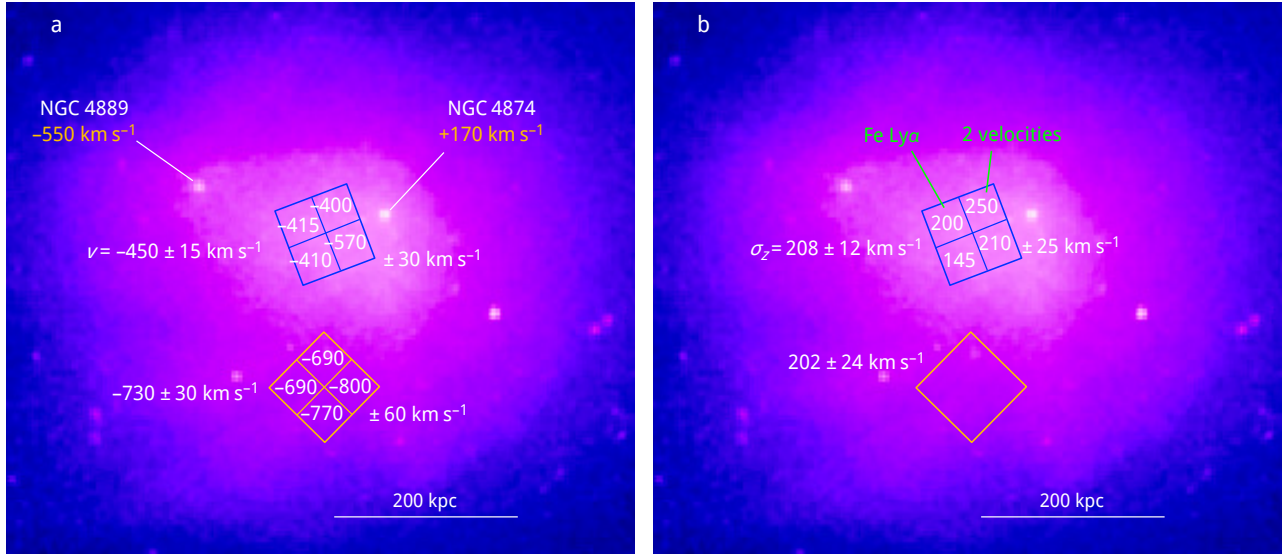


**Figure 3.** *XRISM* Resolve measurements of (a) the LOS velocities relative to the mean velocity of cluster member galaxies and (b) LOS velocity dispersion, overlaid on the *XMM-Newton* image. Uncertainties are statistical  $1\sigma$ . The values to the left of the fields represent the entire  $3' \times 3'$  field, while the values inside the FOV pertain to the  $1.5'$  quadrants, for which the relatively small PSF smearing effect is not included. The two brightest galaxies are marked along with their relative LOS velocities. Green labels mark the quadrants discussed in §§3.2–3.3.

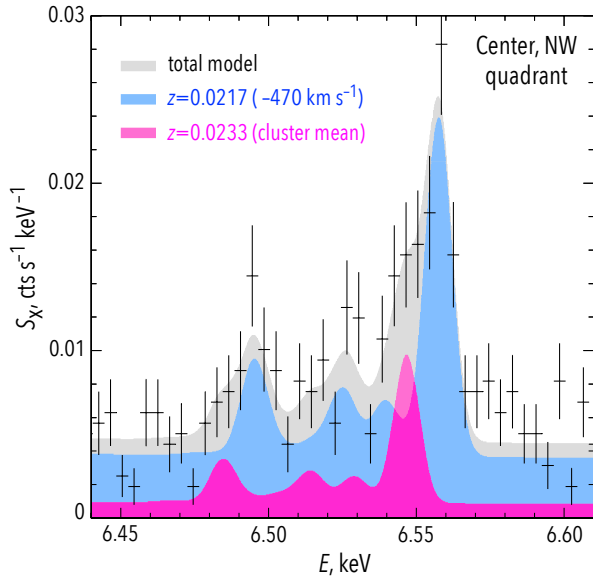


**Figure 4.** The spectrum for the NW quadrant of the Center field (the one with the highest velocity dispersion, see Fig. 3b). Only the Fe-He $\alpha$  line complex is displayed, binned by 4 eV. Two velocity components are needed to model the line profile. The main component (blue) is blueshifted from the cluster mean by  $470 \text{ km s}^{-1}$ , while the additional component (magenta) is at the cluster optical velocity and contributes  $22 \pm 7\%$  of the emission measure.

### 3.3. Fe Ly $\alpha$ anomaly

A detailed look at the spectra in the Center quadrants reveals an apparent excess of the Fe Ly $\alpha_2$  line flux over the model in the NE quadrant (Fig. 5). The other three quadrants,

or the South region (Fig. 2b), do not show such anomaly. An additional flux in this line component is required at a  $\sim 3\sigma$  significance; given that we searched 5 spectra for this signal (four Center quadrants and South), this corresponds to a detection at a  $\sim 98\%$  statistical confidence level. The line cannot be attributed to an additional velocity component. Resonant scattering in the Fe Ly $\alpha$  lines, proposed to explain a modified  $\alpha_1/\alpha_2$  flux ratio (compared to the theoretically expected 2:1) in some other sources (e.g., Gunasekera et al. 2024), has negligible optical depth in Coma (e.g., Sazonov et al. 2002). There is nothing anomalous at this location in the X-ray (*Chandra* or *XMM-Newton*), optical, or radio images of the cluster. Interestingly, the spectrum of A2029 (*XRISM* Collab. 2025a) exhibits a similar anomaly, although with lower amplitude. Physical explanations for this anomaly will be explored in future work.

## 4. DISCUSSION

### 4.1. Velocity dispersion and kinetic pressure

Assuming isotropic velocities, the observed LOS velocity dispersions (Table 1) correspond to Mach numbers of  $M_{3D} = \sqrt{3}M_z = 0.24 \pm 0.015$  and  $0.25 \pm 0.03$  for the small-scale gas motions in the Center and South pointings, respectively. The fraction of kinetic pressure in total ICM pressure, estimated as (e.g., Eckert et al. 2019)

$$\frac{p_{\text{kin}}}{p_{\text{tot}}} = \left(1 + \frac{3}{\gamma M_{3D}^2}\right)^{-1}, \quad (1)$$

is  $3.1 \pm 0.4\%$  and  $3.3 \pm 0.8\%$  for the Center and South sight-lines. This estimate does not include pressure contributions from bulk velocities, as it is based on local dispersions relative to the local bulk velocities in the C and S fields; how-

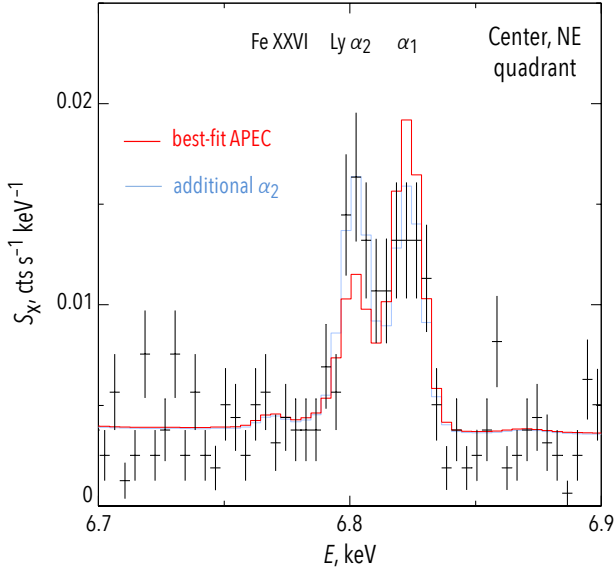


**Figure 5.** The spectrum from the NE quadrant of the Center field around the Fe-Ly $\alpha$  line, binned by 4 eV. The red line shows a BAPEC model fit in the interval shown in Fig. 2 (including Fe He $\alpha$  and Ly $\alpha$  lines). An excess is observed in the Ly $\alpha_2$  component. The blue line shows a fit with additional flux in this line, required at  $\sim 3\sigma$  significance.

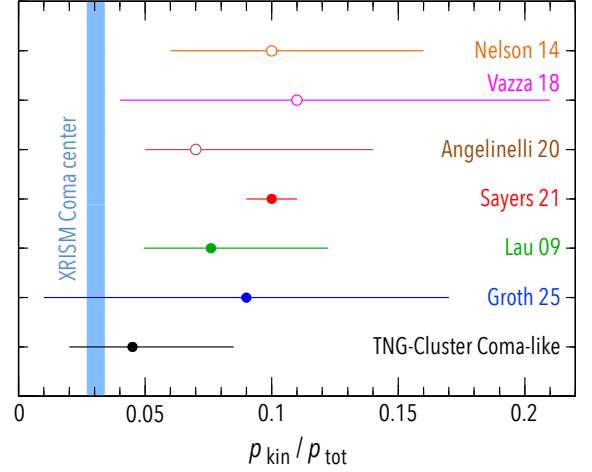
ever, it does use the full velocity dispersion without attempting to separate large-scale and small-scale variations along the LOS. Notably, this pressure ratio is similar to  $p_{\text{kin}}/p_{\text{tot}} = 2.6 \pm 0.3\%$  that *XRISM* measured (in a similar manner) in the cool core of A2029 (*XRISM Collab. 2025a*), one of the most relaxed clusters known.

Figure 6 compares this kinetic pressure in the Coma Center to predictions from several cosmological simulations, selecting sightlines through the cluster center and estimating  $p_{\text{kin}}$  based on the LOS velocity dispersions, as done for Coma, while choosing Coma-like disturbed clusters whenever possible (see Appendix B).

Our measured velocity dispersion is at the lower end of, or in many cases lower than, the simulation predictions. One might expect that the finite numerical resolution in cosmological simulations would lead to an underestimation of ICM velocities on small linear scales; however, we observe the opposite. The dispersion in the cool core of A2029 is also found to be on the low end of predictions (*XRISM Collab. 2025a*). Upcoming *XRISM* observations of other clusters will determine whether this is more than a statistical fluctuation.

#### 4.2. Velocities of gas versus galaxies

The galaxy velocity distribution in the central  $r < 20' \sim 0.6$  Mpc region of the cluster (which excludes the well-separated infalling group centered on NGC 4839) is well described by a single Gaussian (Colless & Dunn 1996; see our updated velocity histogram in Fig. 7). The two BCGs exhibit a large LOS velocity difference, and several small subgroups are de-



**Figure 6.** The *XRISM* value of  $p_{\text{kin}}/p_{\text{tot}}$  for Coma, derived from the central line width, is compared with predictions from several cosmological simulations. Open symbols represent all clusters, while filled symbols select only the disturbed Coma-like clusters. For TNG-Cluster, there is an additional selection based on cluster mass and weighting by X-ray emission measure (see Appendix B). The horizontal intervals show the 16<sup>th</sup>–84<sup>th</sup> percentiles of the simulated cluster populations. The measured value is at the low end of the predictions.

tected in the  $(\alpha, \delta, z)$  distribution of the cluster galaxies in the cluster central region (e.g., Healy et al. 2021), but no prominent substructure indicates an ongoing major merger along the line of sight. It is therefore puzzling why the gas has such a large LOS velocity offset from the cluster galaxies. The velocities in both *XRISM* pointings are closer to that of the secondary BCG, NGC 4889 (Fig. 3a), rather than the main BCG NGC 4874 (which is nearer to the X-ray centroid, the galaxy velocity mean, and the main peak of the mass map in Okabe et al. 2014), as previously suggested by Sanders et al. (2020). As noted above (Fig. 4), there is only a small amount of gas along the sight line near NGC 4874 that matches that galaxy’s velocity. Contrary to the expected scenario of gas and galaxies in approximate hydrostatic equilibrium, our measurements indicate a wind of gas with low random internal motions ( $M_{\text{ID}} = 0.14$ ) flowing through the galaxies at a relatively high speed,  $M_{\text{ID}} = 0.3–0.5$ . This picture is based on data from only two locations in the core and may change as more sight lines are sampled by *XRISM*.

#### 4.3. Velocity power spectrum

The ICM is primarily heated by thermalizing the kinetic energy of gas released during cluster mergers and matter infall, which create shocks and turbulence. The physics of this energy conversion is encoded in the amplitude of the cluster gas velocity variations,  $\mathbf{v}(\mathbf{x})$ , as a function of the length scale  $\ell$  (or wavenumber  $k \equiv 1/\ell$ ). This can be quantified by a power spectrum  $P(k) \equiv |\tilde{v}_z(\mathbf{k})|^2$ , where  $\tilde{v}_z$  is the Fourier transform of one component of the velocity field  $v_z$ ,  $\mathbf{k}$  is the 3D

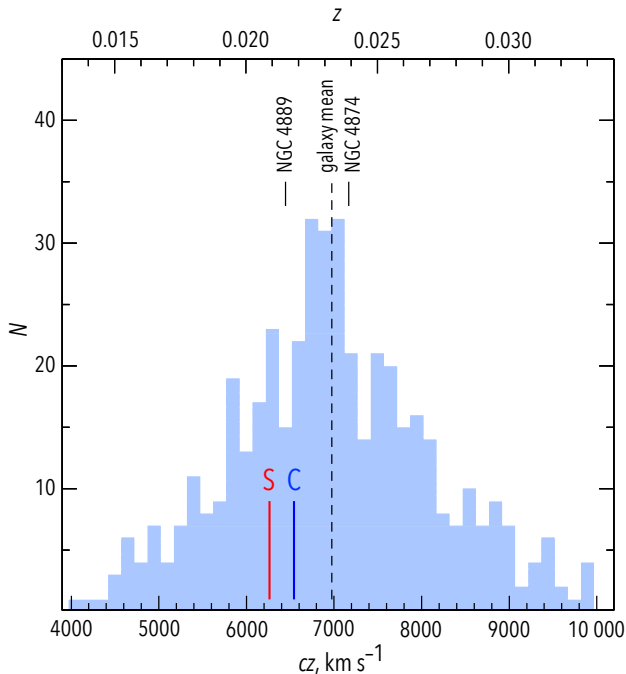


**Figure 7.** A histogram of velocities of cluster member galaxies within  $r < 20'$  from the Coma X-ray center, retrieved from SDSS, DESI, and NED (2019) archival data. The gas velocities measured with *XRISM* for the Center and South fields (marked C and S, respectively) are offset from the cluster galaxy mean. The two main BCGs are marked; NGC 4874 is located near the Center field.

wavevector, and (assuming isotropy of the power spectrum of the velocity field)  $k \equiv |\mathbf{k}|$ .

Gas motions are injected on a large linear scale  $\ell_{\text{inj}}$  by mechanical disturbances (such as cluster collisions, buoyant AGN bubbles, or random galaxy motions); these motions randomize, generate velocity variations on smaller scales, and dissipate (mostly into heat) at a scale  $\ell_{\text{dis}}$  determined by the microphysics of the ICM. In a steady state, the power spectrum attains a characteristic shape that can be described by:

$$P(k) = P_0 [1 + (k\ell_{\text{inj}})^2]^{\alpha/2} \exp[-(k\ell_{\text{dis}})^2], \quad (2)$$

where  $P_0$  is the normalization. In the Kolmogorov (1941) model, the spectrum in the inertial range (between  $\ell_{\text{inj}}$  and  $\ell_{\text{dis}}$ ) has a power law slope  $\alpha = -11/3$ , for which the flux of kinetic energy down the cascade is independent of the scale.

With two *XRISM* pointings  $6'$  apart, whose spectral line positions provide average LOS velocities in  $1.5'$  quadrants and whose line widths average the LOS velocity variations over a range of scales (including the smallest ones that *XRISM* cannot resolve in the sky plane), we can constrain  $P(k)$ . This can be achieved by constructing a velocity structure function (VSF), which quantifies the LOS velocity variation as a function of separation in the sky plane and is directly related to  $P(k)$  (Appendix A). The differences between velocities in the Center quadrants (Fig. 3) are used to evaluate

VSF( $r$ ) at  $r \sim 1.8'$ . The velocity for the entire South pointing is subtracted from each Center quadrant to construct another VSF bin at  $r \sim 6'$  (statistical uncertainties in the South quadrants are twice as large as those in the Center, so we chose not to use them.)

For this exploratory exercise, we treat the large gas velocities relative to the galaxies in our two pointings as another velocity difference at a larger scale. We can reasonably assume that the gas and galaxies fill the same potential well and have the same cluster-averaged velocities, and use the galaxy average as a substitute for the gas average. We therefore use the mean of the S and C velocity offsets from the average of cluster galaxies,  $-590 \text{ km s}^{-1}$ , to construct a VSF point at  $r = 1 \pm 0.5 \text{ Mpc}$  ( $r = 35'$ ); given all the uncertainties, the exact linear scale is not critical. The resulting VSF is shown in Fig. 8a, along with the dispersion values for the two pointings.

We model these data with a velocity power spectrum (eq. 2) as described in Appendix A. Key details are: (a) We do not separate turbulence from bulk motions (as in, e.g. Vazza et al. 2012); our eq. (2) describes the total velocity field. (b) Model velocities are weighted by the cluster 3D X-ray emission measure distribution, for which we use a symmetric  $\beta$ -model (Briel et al. 1992) for simplicity. (c) Because the two *XRISM* pointings sample the cluster sparsely, each VSF linear scale is probed by at most a few velocity differences. It is possible that they are outliers, but we have to treat them as representative of the mean of the random velocity field. Additionally, the largest scales of interest are comparable to the size of the cluster, so regardless of *XRISM* coverage, there may only be a couple of large eddies in the entire cluster. These considerations lead to a large, but quantifiable, “cosmic variance” uncertainty in our modeling (ZuHone et al. 2016; Appendix A). Currently, this is the dominant uncertainty limiting our conclusions.

We fix  $\ell_{\text{inj}} = 1 \text{ Mpc}$  (a logical first guess for a merger) and  $\ell_{\text{dis}} = 1 \text{ kpc}$  (essentially zero, as it is well below *XRISM* resolution) and fit the VSF data with a Kolmogorov ( $\alpha = -11/3$ ) model, with normalization as the only free parameter. This model is shown by the red dashed line in Fig. 8a, while the red band combines the 68% statistical uncertainty of the data and the cosmic variance for the model into a single uncertainty interval. The model fits the *velocities* well ( $\chi^2 = 0.2$  for 2 d.o.f.); however, it predicts a dispersion,  $\sigma_z = 475 \pm 53 \text{ km s}^{-1}$ , far exceeding the observed line widths (Fig. 8a inset). If we fit the VSF and dispersions together using the Kolmogorov slope, we obtain a poor fit with  $\chi^2 = 13.0$  for 4 d.o.f. — there is a clear tension between the velocities and the dispersions, indicating a need for a steeper  $P(k)$  model. The green line with the blue band in Fig. 8 shows one such model, with  $\alpha = -8$  and the same  $\ell_{\text{inj}}$  and  $\ell_{\text{dis}}$ . It fits better with  $\chi^2 = 1.6$  for 3 d.o.f.; the F-test indicates a 98% confidence that the slope must be steeper than Kolmogorov. The 68% constraint on the slope is  $\alpha < -4.8$ .

Another way to steepen the spectrum is to use a large value for  $\ell_{\text{dis}}$ ; an indistinguishable fit to the VSF and dispersions is achieved for  $\ell_{\text{dis}} = 1000 \text{ kpc}$ , or  $\ell_{\text{dis}} > 240 \text{ kpc}$  at 68% confidence. (The best-fit values for  $\alpha$  and  $\ell_{\text{dis}}$  are merely the upper

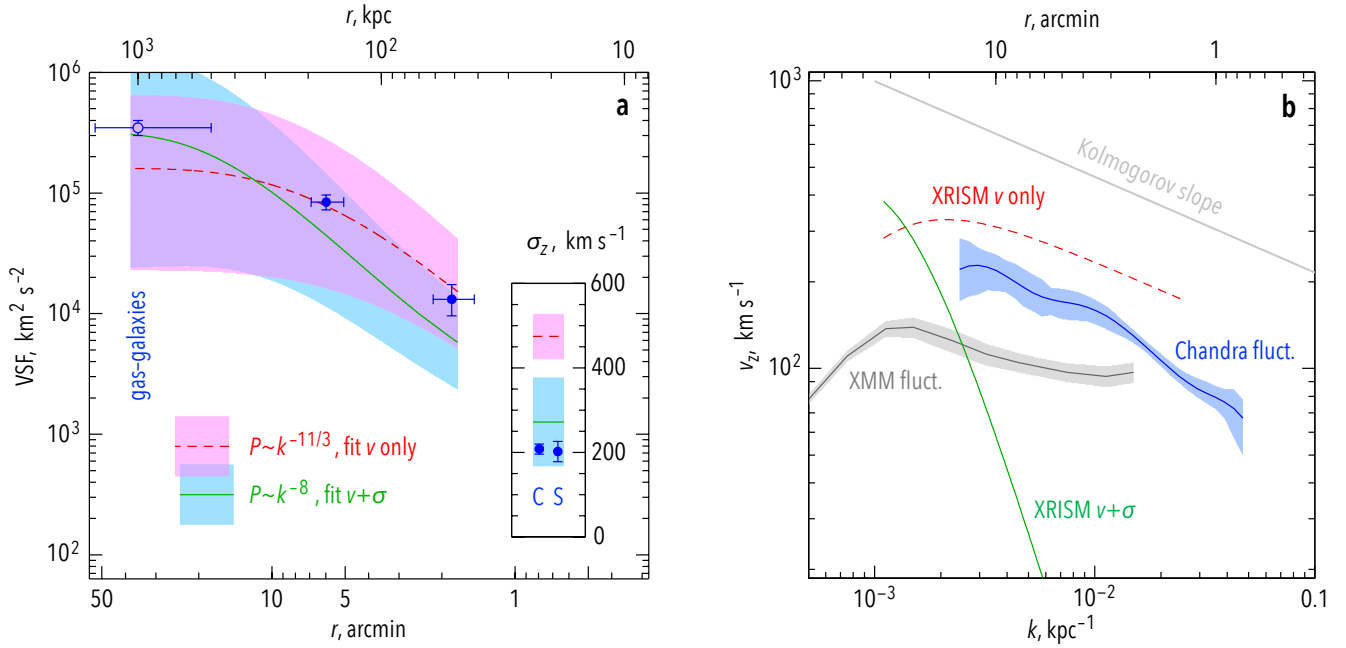


**Figure 8.** Turbulence power spectrum inferred from the observed gas velocity differences and dispersions. (a) The velocity structure function is shown by blue crosses. The two velocity dispersions are shown in the inset by blue symbols. The gas-galaxy offset (see text) is included as a velocity difference at 1 Mpc (open symbol). The red dashed line fits a Kolmogorov spectrum with  $\ell_{\text{inj}}=1$  Mpc and  $\ell_{\text{dis}}=1$  kpc to the VSF points only; it significantly overestimates the line broadening. The green line shows a model with a steeper slope that fits all *XRISM* data (velocity differences and dispersions). The color error bands for the models include the 68% cosmic variance uncertainty and the measurement statistical errors (the latter are also shown as error bars on data points for illustration). The horizontal bars show approximate bin sizes. (b) Velocity amplitudes for the same two power spectra. Spectra from X-ray surface brightness fluctuation analyses of *Chandra* and *XMM-Newton* images are shown for comparison (Zhuravleva et al. 2019; Sanders et al. 2020) (note these are not directly comparable; see text).

bounds of our trials, where the goodness of fit depends only weakly on the exact value of the parameter, and so they do not carry as much physical significance as their 68% bounds.)

We note that the LOS velocity dispersion incorporates contributions from all linear scales (weighted by the X-ray emission along the LOS), not just from small scales. When fit to the velocity and dispersion data, our steeper-spectrum models are more consistent with the low observed dispersions largely because the predicted scatter of  $\sigma_z$  among different sightlines (the cosmic variance) is higher for steep-spectrum models (Fig. 8a inset), making it less improbable to encounter random deviations as low as the observed  $\sigma_z$ . If future pointings yield similarly low dispersions, this model will become less tenable.

Velocity amplitudes for the Kolmogorov fit to the VSF and the steep-slope fit to all data are shown in Fig. 8b (the high- $\ell_{\text{dis}}$  model is qualitatively similar to the steep-slope one and is not shown). The models exhibit similar amplitudes around  $\ell \sim 500$  kpc sampled by the bulk velocities but diverge at smaller scales. The figure also shows two indirect estimates of the velocity variations derived from X-ray surface brightness fluctuations in *Chandra* and *XMM-Newton* images (Churazov et al. 2012; Zhuravleva et al. 2019; Sanders et al. 2020), assuming that the velocity variations are proportional to the density fluctuations on scale  $k$ :  $\delta\rho_k/\rho = \eta v_{z,k}/c_s$

with  $\eta \approx 1$  (Zhuravleva et al. 2014, 2023). The *Chandra* result pertains to the Coma core and can be approximately compared with *XRISM* measurements in the core (although *XRISM* does not sample the entire *Chandra* region). The *Chandra* spectrum, when integrated along the LOS weighted with the X-ray emissivity (similarly to our  $P(k)$  modeling, see Appendix A), would yield  $\sigma_z = 300$  km s $^{-1}$ , a factor  $\sim 1.5$  higher than the *XRISM* dispersion measurements, which falls within the large uncertainties of this indirect method expected for merging clusters (Zhuravleva et al. 2023). The *XMM-Newton* fluctuation spectrum does not exceed the observed  $\sigma_z$ , although the *XMM-Newton* spectrum is derived for the entire cluster ( $r = 1.5$  Mpc) and is not directly comparable to the *XRISM* measurements in the core.

The *Chandra* finding that the Kolmogorov slope extends to high  $k$  has been interpreted as evidence for a very low effective isotropic viscosity in the ICM (Zhuravleva et al. 2019). The shape of our preferred  $P(k)$  model is qualitatively very different from both fluctuation-based results. However, with the available sparse data, we could only consider the simplest family of spectra (eq. 2) and cannot rule out the possibility that a more complex shape would fit all *XRISM* data and be more similar in shape — even if not in amplitude — to the fluctuation results at higher  $k$ . It is thus crucial to validate the fluctuations-based spectral shape with *XRISM*

measurements in the range of scales where the instruments overlap ( $1.5' - 15'$  or  $k = 0.002 - 0.02$ ) and to confirm that the X-ray surface brightness fluctuations indeed return the ICM velocities. This would require a more complete coverage of the cluster core with multiple *XRISM* pointings, aimed at (a) sampling more scales and (b) reducing the cosmic variance uncertainties for the VSF and line widths.

#### 4.4. Velocity spectrum interpretation

While the exact shape of the velocity power spectrum is still uncertain, it is clear from *XRISM* results that it is steep, exhibiting relatively lower velocities at small scales compared to a steady-state Kolmogorov model of turbulence. Two broad possibilities exist: (a) fast dissipation of motions on intermediate linear scales, preventing power from reaching small scales, or (b) a transient state, where random motions generated at large scales have not yet cascaded down to small scales. The first possibility would require a dissipation scale,  $\ell_{\text{dis}} \gtrsim 240$  kpc, much larger than the Coulomb collision mean free path in the Coma core,  $\lambda \approx 10$  kpc, and consequently a very high effective viscosity of the ICM. The second possibility requires an ongoing major merger, as the velocities should cascade on a timescale of order the large eddy turnover time,  $2 - 3$  Gyr. However, the galaxy velocity distribution does not indicate a strong merger (see §4.2). Both possibilities have challenges but remain open for now, pending better constraints on the shape of the spectrum.

The notion that cosmic ray electrons responsible for giant radio halos in clusters (including Coma) are reaccelerated by ICM turbulence depends on the turbulence spectrum extending to very small scales, where acceleration occurs (Brunetti & Jones 2014). If motions dissipate at large scales, as happens in one of our possibilities, this explanation may become problematic. This underscores the importance of accurately determining the shape of the Coma velocity spectrum.

## 5. SUMMARY

Using *XRISM* Resolve, we conducted exploratory measurements of ICM velocities in two  $3' \times 3'$  regions of the Coma cluster. We detected a high-velocity wind blowing through the galaxies, but the velocity dispersion is relatively low in both regions, implying a velocity power spectrum with an effective slope steeper than that in the classic Kolmogorov model of steady-state turbulence. This raises questions about the dynamical state of the cluster and the physics of the ICM.

Answers may be found in a more precise shape of the power spectrum.

## ACKNOWLEDGMENTS

The results presented above are made possible by over three decades of work by the team of scientists and engineers who created a microcalorimeter array for X-rays and overcame enormous setbacks. We gratefully acknowledge the entire *XRISM* team's effort to build, launch, calibrate, and operate this observatory. We thank the referee for useful comments. Part of this work was supported by the U.S. Department of Energy by Lawrence Livermore National Laboratory under Contract DE-AC52-07NA27344, and by NASA under contracts 80GSFC21M0002 and 80GSFC24M0006 and grants 80NSSC20K0733, 80NSSC18K0978, 80NSSC20K0883, 80NSSC20K0737, 80NSSC24K0678, 80NSSC18K1684, 80NSSC23K0650, and 80NNSC22K1922. Support was provided by JSPS KAKENHI grant numbers JP23H00121, JP22H00158, JP22H01268, JP22K03624, JP23H04899, JP21K13963, JP24K00638, JP24K17105, JP21K13958, JP21H01095, JP23K20850, JP24H00253, JP21K03615, JP24K00677, JP20K14491, JP23H00151, JP19K21884, JP20H01947, JP20KK0071, JP23K20239, JP24K00672, JP24K17104, JP24K17093, JP20K04009, JP21H04493, JP20H01946, JP23K13154, JP19K14762, JP20H05857, and JP23K03459, the JSPS Core-to-Core Program, JPJSCA20220002, and the Strategic Research Center of Saitama University. LC acknowledges support from NSF award 2205918. CD acknowledges support from STFC through grant ST/T000244/1. LG acknowledges support from Canadian Space Agency grant 18XARMSTMA. NO acknowledges partial support by the Organization for the Promotion of Gender Equality at Nara Women's University. MS acknowledges support by the RIKEN Pioneering Project Evolution of Matter in the Universe (r-EMU) and Rikkyo University Special Fund for Research (Rikkyo SFR). AT acknowledges support from the Kagoshima University post-doctoral research program (KU-DREAM). SY acknowledges support by the RIKEN SPDR Program. IZ acknowledges partial support from the Alfred P. Sloan Foundation through the Sloan Research Fellowship. DN acknowledges funding from the Deutsche Forschungsgemeinschaft (DFG) through an Emmy Noether Research Group (grant number NE 2441/1-1).

## APPENDIX

### A. MODELING VELOCITY STRUCTURE FUNCTION AND ITS SCATTER

Under the assumptions of isotropy and homogeneity, all three components of the gas velocity field  $\mathbf{v}(\mathbf{x})$  have the same power spectrum  $P$  and  $P(\mathbf{k}) = P(k)$ . We further assume that the velocity field can be represented by a Gaussian random field with a power spectrum  $P(k)$  given by eq. (2).

What is measured by *XRISM* is not  $\mathbf{v}(\mathbf{x})$  but the first ( $\mu_z$ ) and second ( $\sigma_z$ ) moments of the projected velocity component aligned with the line of sight, given by (assuming the line of sight is along the  $z$ -axis in a Cartesian coordinate system):

$$\mu_z(x, y) = \int v_z(\mathbf{x}) \varepsilon(\mathbf{x}) dz \quad (\text{A1})$$

$$\sigma_z^2(x, y) = \int v_z^2(\mathbf{x}) \varepsilon(\mathbf{x}) dz - \mu_z^2 \quad (\text{A2})$$

where

$$\varepsilon(\mathbf{x}) = \frac{\text{EM}(\mathbf{x})}{\int \text{EM}(\mathbf{x}) dz} \quad (\text{A3})$$

is the emission measure EM normalized by its LOS integral. We have assumed that the Coma ICM is approximately isothermal, so the velocity weighting is independent of the gas temperature. Consequently, the 2D power spectrum of  $\mu_z$  is related to the 3D spectrum  $P$  as

$$P_{2D}(k) = \int P\left(\sqrt{k^2 + k_z^2}\right) P_\varepsilon(k_z) dk_z, \quad (\text{A4})$$

where  $P_\varepsilon(k_z)$  is the 1D power spectrum of the normalized emission measure (Zhuravleva et al. 2012; ZuHone et al. 2016; Clerc et al. 2019).

It is not possible to measure  $P_{2D}$  directly from a limited set of pointings such as ours; however, a more easily computed quantity, the second-order structure function  $\text{VSF}(r)$  of the bulk velocity, is related to the power spectrum. As shown by ZuHone et al. (2016) and Clerc et al. (2019):

$$\text{VSF}(r) \equiv \langle |\mu_z(\boldsymbol{\chi} + \mathbf{r}) - \mu_z(\boldsymbol{\chi})|^2 \rangle = 4\pi \int_0^\infty [1 - J_0(2\pi kr)] P_{2D}(k) k dk, \quad (\text{A5})$$

where  $\mathbf{r}$  is the distance vector on the sky between a pair of points, and the average is taken over all points with position  $\boldsymbol{\chi}$ .  $J_0$  is a Bessel function of the first kind of order zero. It can similarly be shown that the LOS velocity dispersion  $\sigma_z$  is related to  $P$  by

$$\sigma_z^2 = \int P(k) [1 - P_\varepsilon(k_z)] d^3\mathbf{k}. \quad (\text{A6})$$

In light of these relationships, we can constrain the parameters of the power spectrum  $P(k)$  from the structure function  $\text{VSF}(r)$  calculated from the line shift measurements, and the measured velocity broadening  $\sigma_z$ . In practice, these formulas need to be corrected for the shape of the pixelization, region shapes, and PSF (Clerc et al. 2019), which we do by replacing  $P_\varepsilon$  with  $P_\varepsilon P_{\text{inst}}$ , where  $P_{\text{inst}}$  is the power spectrum of these instrumental effects. To model the PSF effect, we use a Gaussian with  $\sigma = 34''$  (HPD=1.3'), which has the same scattering fraction for the adjacent 1.5' square regions and flat brightness distribution as the actual Resolve PSF. This approximation is adequate given other significant uncertainties.

The construction of  $\text{VSF}(r)$  must account for the statistical, systematic, and cosmic variance uncertainties of the velocities. As noted in §3.2, the statistical error on the bulk velocity  $\mu_z$  is  $\sigma_{\text{stat}} = 30 \text{ km s}^{-1}$  for the four quadrants in the central pointing and for the entire southern pointing, and the systematic error (from gain uncertainty) is  $\sigma_{\text{sys}} \lesssim 15 \text{ km s}^{-1}$  (§2). As shown by ZuHone et al. (2016) and Cucchetti et al. (2019), the observed structure function  $\text{VSF}'(r)$  is biased by these errors as:

$$\text{VSF}'(r) = \text{VSF}(r) + 2\sigma_{\text{stat}}^2 + 2\sigma_{\text{sys}}^2. \quad (\text{A7})$$

Additionally, the observed velocity field in Coma represents one possible realization of the random field model with power spectrum given by  $P(k)$ . To determine the expected sample, or ‘‘cosmic,’’ variance on  $\text{VSF}(r)$ , we adopt a procedure similar to ZuHone et al. (2016) and construct 3D cubes of Gaussian random velocity fields using a range of values for  $P_0$ ,  $\ell_{\text{inj}}$ ,  $\ell_{\text{dis}}$ , and  $\alpha$ . For a given set of model parameters, we perform 1500 realizations of the 3D velocity field and project it using eqs. A1-A3 to obtain realizations of  $\mu_z$  and  $\sigma_z$ . From these realizations, we compute  $\text{VSF}'(r)$  using eq. A7 and determine the asymmetric sample variance (i.e., taking the variance of deviations above and below the mean separately) on  $\text{VSF}'(r)$ . We find that, to an adequate precision, the combined statistical and sample variance on  $\text{VSF}'(r)$  follows a power-law distribution, which we use to compute the total variance for any value of  $\text{VSF}'(r)$ . These total variances and the mean values of  $\text{VSF}'(r)$  for each set of the  $P(k)$  model parameters are then compared to the observed VSF values to calculate and minimize  $\chi^2$ . For the sample variance on  $\sigma_z$ , we use eq. 7 from Clerc et al. (2019). We validated this model fitting procedure using random realizations of the velocity field, from which we successfully derived the input parameters.

## B. PREDICTIONS FOR KINETIC PRESSURE FROM COSMOLOGICAL SIMULATIONS

To compare *XRISM* observations with theoretical predictions for ICM kinematics, we primarily use the TNG-Cluster suite of cosmological simulations (Nelson et al. 2024), selecting Coma-like systems and emulating *XRISM* measurements of gas velocities for direct comparison with observations. TNG-Cluster consists of 352 high-resolution MHD re-simulations of clusters extracted from a 1 Gpc parent box of a dark matter-only simulation, including radiative cooling, magnetic fields, and stellar and AGN feedback processes (Nelson et al. 2019; Pillepich et al. 2018b,a).

We identify Coma-like systems among the simulated clusters at  $z=0$  based on halo mass and core properties, selecting clusters with  $M_{200c} \approx 10^{15.1-15.4} M_{\odot}$ , which corresponds to the Coma mass range (Ho et al. 2022). From those, we select only non-cool-core systems with central cooling times exceeding 7.7 Gyr (Lehle et al. 2024). In TNG-Cluster, central cooling time is strongly correlated with cluster’s dynamical state. We verify that non-cool-core clusters are the most disturbed, typically undergoing mergers. We end up with a sample of 14 Coma-like systems. For each, we compute the emission-weighted velocity dispersion and temperature for the central pointing within a 90 kpc square aperture, corresponding to the Resolve FOV at the Coma redshift. We consider three projections along the  $x$ ,  $y$ , and  $z$  directions of the simulation domain as separate clusters. The LOS velocity dispersion and temperature for the central pointing are given by

$$\sigma_{\text{los}}^2 = \frac{\sum_i \varepsilon_i v_{\text{los},i}^2}{\sum_i \varepsilon_i} - \left( \frac{\sum_i \varepsilon_i v_{\text{los},i}}{\sum_i \varepsilon_i} \right)^2, \quad (\text{B8})$$

and

$$T = \frac{\sum_i \varepsilon_i T_i}{\sum_i \varepsilon_i}, \quad (\text{B9})$$

where  $v_{\text{los},i}$  ( $T_i$ ) is the LOS velocity (temperature) of the  $i^{\text{th}}$  gas cell, and  $\varepsilon_i$  is its X-ray emissivity in the 6–8 keV energy range. The X-ray emission is computed using the density, temperature, and metallicity of each simulated gas cell, employing the APEC plasma model (Smith et al. 2001). The computed  $\sigma_{\text{los}}$  and  $T$  are used to calculate the kinetic-to-total pressure ratio  $p_{\text{kin}}/p_{\text{tot}}$  as described in eq. (1).

In addition to the TNG-Cluster predictions, we compare the *XRISM* results with previous numerical studies of the ICM pressure ratio  $p_{\text{kin}}/p_{\text{tot}}$  in cluster cores (Lau et al. 2009; Nelson et al. 2014; Vazza et al. 2018; Angelinelli et al. 2020; Sayers et al. 2021; Groth et al. 2025), as shown in Fig. 6. These predictions are derived from cosmological simulations of massive clusters that utilize various numerical schemes and physical models for the ICM. Unlike our TNG sample, clusters in those studies were not selected to match both of our Coma-like criteria. For simulations presented in Lau et al. (2009); Sayers et al. (2021); Groth et al. (2025), we can extract predictions specific to non-relaxed clusters, whereas the other studies do not distinguish clusters based on their dynamical state. Additionally, the pressure ratios  $p_{\text{kin}}/p_{\text{tot}}$  are not computed using emission-weighted averaging — most present mass-weighted averages, while Sayers et al. (2021) derives the pressure ratio from a three-dimensional triaxial analysis of the cluster mass distribution. Despite these caveats, these studies predict core pressure ratios in the 5–10% range, consistent with the TNG-Cluster predictions, albeit systematically toward the higher end of the TNG-Cluster range.

## REFERENCES

- Andrade-Santos, F., Nulsen, P. E. J., Kraft, R. P., et al. 2013, *ApJ*, 766, 107  
 Angelinelli, M., Vazza, F., Giocoli, C., et al. 2020, *MNRAS*, 495, 864  
 Arnaud, M., Aghanim, N., Gastaud, R., et al. 2001, *A&A*, 365, L67  
 Arnaud, K. A., 1996, *ASPC*, 101, 17  
 Asplund, M., Grevesse, N., Sauval, A. J., et al. 2009, *ARA&A*, 47, 481  
 Bilton, L. E. & Pimblett, K. A. 2018, *MNRAS*, 481, 1507  
 Botteon, A., Brunetti, G., van Weeren, R. J., et al. 2020, *ApJ*, 897, 93  
 Briel, U. G., Henry, J. P., & Boehringer, H. 1992, *A&A*, 259, L31  
 Briel, U. G. & Henry, J. P. 1994, *Nature*, 372, 439  
 Brown, S. & Rudnick, L. 2011, *MNRAS*, 412, 2  
 Brunetti, G. & Jones, T. W. 2014, *Int. J. Modern Phys. D*, 23, 1430007-98  
 Burns, J. O., 1998, *Science*, 280, 400  
 Churazov, E., Forman, W., Jones, C., et al. 2000, *A&A*, 356, 788  
 Churazov, E., Vikhlinin, A., Zhuravleva, I., et al. 2012, *MNRAS*, 421, 1123  
 Churazov, E., Khabibullin, I., Lyskova, N., et al. 2021, *A&A*, 651, A41  
 Clerc, N., Cucchetti, E., Pointecouteau, E., et al. 2019, *A&A*, 629, A143  
 Colless, M. & Dunn, A. M., 1996, *ApJ*, 458, 435  
 Cucchetti, E., Clerc, N., Pointecouteau, E., et al. 2019, *A&A*, 629, A144  
 Eckart, M. E., Brown, G. V., Chiao, M. P., et al. 2024, *Proc. SPIE*, 13093, 130931P  
 Eckart, M. E., et al. 2025, *JATIS*, submitted  
 Eckert, D., Ghirardini, V., Ettori, S., et al. 2019, *A&A*, 621, A40  
 Fabian, A. C., Sanders, J. S., Taylor, G. B., et al. 2006, *MNRAS*, 366, 417  
 Groth, F., Valentini, M., Steinwandel, U. P., et al. 2025, *A&A*, 693, A263  
 Gunasekera, C. M., van Hoof, P. A. M., Tsujimoto, M., et al. 2024, arXiv:2411.15357  
 Healy, J., Blyth, S.-L., Verheijen, M. A. W., et al. 2021, *A&A*, 650, A76  
 Hitomi Collaboration 2016, *Nature*, 535, 117  
 Ho, M., Ntampaka, M., Rau, M. M., et al. 2022, *Nature Astronomy*, 6, 936  
 Ishisaki, Y., Kelley, R. L., Awaki, H., et al. 2022, *Proc. SPIE*, 12181, 121811S  
 Jones, C. & Forman, W. 1999, *ApJ*, 511, 65  
 Kelley, R. L., Akamatsu, H., Azzarello, P., et al. 2016, *Proc. SPIE*, 9905, 99050V  
 Kolmogorov, A. 1941, *Akademiia Nauk SSSR Doklady*, 30, 301  
 Lau, E. T., Kravtsov, A. V., Nagai, D. 2009, *ApJ*, 705, 1129  
 Lehle, K., Nelson, D., Pillepich, A., et al. 2024, *A&A*, 687, A129  
 Markevitch, M. & Vikhlinin, A. 2007, *PhR*, 443, 1  
 McNamara, B. R. & Nulsen, P. E. J. 2007, *ARA&A*, 45, 117  
 NASA/IPAC Extragalactic Database (NED), 2019, <https://doi.org/10.26132/NED1>  
 Nelson, K., Lau, E. T., Nagai, D., et al. 2014, *ApJ*, 792, 25  
 Nelson, D., Springel, V., Pillepich, A., et al. 2019, *Computational Astrophysics and Cosmology*, 6, 2

- Nelson, D., Pillepich, A., Ayromlou, M., et al. 2024, *A&A*, 686, A157
- Okabe, N., Futamase, T., Kajisawa, M., et al. 2014, *ApJ*, 784, 90
- Pillepich, A., Springel V., Nelson, D., et al. 2018, *MNRAS*, 473, 4077
- Pillepich, A., Nelson D., Hernquist, L., et al. 2018, *MNRAS*, 475, 648
- Planck Collaboration, Ade, P. A. R., Aghanim, N., et al. 2013, *A&A*, 554, A140
- Porter, F. S., Kilbourne, C. A., Chiao, M., et al. 2024, *Proc. SPIE*, 13093, 130931K
- Sanders, J. S., Fabian, A. C., Churazov, E., et al. 2013, *Science*, 341, 1365
- Sanders, J. S., Fabian, A. C., Sun, M., et al. 2014, *MNRAS*, 439, 1182
- Sanders, J. S., Dennerl, K., Russell, H. R., et al. 2020, *A&A*, 633, A42
- Sayers, J., Mauro, S., Ettori, S., et al. 2021, *MNRAS*, 505, 4338
- Sazonov, S. Y., Churazov, E. M., & Sunyaev, R. A. 2002, *MNRAS*, 333, 191
- Schuecker, P., Finoguenov, A., Miniati, F., et al. 2004, *A&A*, 426, 387
- Smith, R. K., Brickhouse, N. S., Liedahl, D. A., et al. 2001, *ApJ*, 556, L91
- Takahashi, T., Kokubun, M., Mitsuda, K., et al. 2016, *Proc. SPIE*, 9905, 99050U
- Tashiro, M., Maejima, H., Toda, K., et al. 2020, *Proc. SPIE*, 11444, 1144422
- Vazza, F., Roediger, E., & Brüggem, M. 2012, *A&A*, 544, A103
- Vazza, F., Angelinelli, M., Jones, T. W., et al. 2018, *MNRAS Letter*, 481, L120
- Vikhlinin, A., Forman, W., & Jones, C. 1997, *ApJL*, 474, L7
- Vikhlinin, A., Markevitch, M., Forman, W., et al. 2001, *ApJL*, 555, L87
- XRISM* Collaboration 2025a, *ApJL*, 982, L5
- XRISM* Collaboration 2025b, *Nature* 638, 365
- Zhuravleva, I., Churazov, E., Kravtsov, A., et al. 2012, *MNRAS*, 422, 2712
- Zhuravleva, I., Churazov, E. M., Schekochihin, A. A., et al. 2014, *ApJL*, 788, L13
- Zhuravleva, I., Churazov, E., Schekochihin, A. A., et al. 2019, *Nature Astronomy*, 3, 832
- Zhuravleva, I., Chen, M. C., Churazov, E., et al. 2023, *MNRAS*, 520, 5157
- ZuHone, J. A., Markevitch, M., & Zhuravleva, I. 2016, *ApJ*, 817, 110

## All Authors and Affiliations

### XRISM COLLABORATION:

MARC AUDARD<sup>1</sup> HISAMITSU AWAKI<sup>2</sup> RALF BALLHAUSEN<sup>3,4,5</sup> AYA BAMBA<sup>6</sup> EHUD BEHAR<sup>7</sup> ROZENN BOISSAY-MALAQUIN<sup>8,4,5</sup>  
LAURA BRENNEMAN<sup>9</sup> GREGORY V. BROWN<sup>10</sup> LIA CORRALES<sup>11</sup> ELISA COSTANTINI<sup>12</sup> RENATA CUMBE<sup>4</sup> MARIA DIAZ TRIGO<sup>13</sup>  
CHRIS DONE<sup>14</sup> TADAYASU DOTANI<sup>15</sup> KEN EBISAWA<sup>15</sup> MEGAN E. ECKART<sup>10</sup> DOMINIQUE ECKERT<sup>1</sup> SATOSHI EGUCHI<sup>16</sup>  
TERUAKI ENOTO<sup>17</sup> YUICHIRO EZOE<sup>18</sup> ADAM FOSTER<sup>9</sup> RYUICHI FUJIMOTO<sup>15</sup> YUTAKA FUJITA<sup>18</sup> YASUSHI FUKAZAWA<sup>19</sup>  
KOTARO FUKUSHIMA<sup>15</sup> AKIHIRO FURUZAWA<sup>20</sup> LUIGI GALLO<sup>21</sup> JAVIER A. GARCÍA<sup>4,22</sup> LIYI GU<sup>12</sup> MATTEO GUAINAZZI<sup>23</sup>  
KOUICHI HAGINO<sup>6</sup> KENJI HAMAGUCHI<sup>8,4,5</sup> ISAMU HATSUKADE<sup>24</sup> KATSUHIRO HAYASHI<sup>15</sup> TAKAYUKI HAYASHI<sup>8,4,5</sup>  
NATALIE HELL<sup>10</sup> EDMUND HODGES-KLUCK<sup>4</sup> ANN HORNSCHMEIER<sup>4</sup> YUTO ICHINOHE<sup>25</sup> DAIKI ISHI<sup>15</sup> MANABU ISHIDA<sup>15</sup>  
KUMI ISHIKAWA<sup>18</sup> YOSHITAKA ISHISAKI<sup>18</sup> JELLE KAASTRA<sup>12,26</sup> TIMOTHY KALLMAN<sup>4</sup> ERIN KARA<sup>27</sup> SATORU KATSUDA<sup>28</sup>  
YOSHIAKI KANEMARU<sup>15</sup> RICHARD KELLEY<sup>4</sup> CAROLINE KILBOURNE<sup>4</sup> SHUNJI KITAMOTO<sup>29</sup> SHOHO KOBAYASHI<sup>30</sup>  
TAKAYOSHI KOHMURA<sup>31</sup> AYA KUBOTA<sup>32</sup> MAURICE LEUTENEGGER<sup>4</sup> MICHAEL LOEWENSTEIN<sup>3,4,5</sup> YOSHITOMO MAEDA<sup>15</sup>  
MAXIM MARKEVITCH<sup>4</sup> HIRONORI MATSUMOTO<sup>33</sup> KYOKO MATSUSHITA<sup>30</sup> DAN MCCAMMON<sup>34</sup> BRIAN MCNAMARA<sup>35</sup>  
FRANÇOIS MERNIER<sup>36</sup> ERIC D. MILLER<sup>27</sup> JON M. MILLER<sup>11</sup> IKUYUKI MITSUISHI<sup>37</sup> MISAKI MIZUMOTO<sup>38</sup>  
TSUNEFUMI MIZUNO<sup>39</sup> KOJI MORI<sup>24</sup> KOJI MUKAI<sup>8,4,5</sup> HIROSHI MURAKAMI<sup>40</sup> RICHARD MUSHOTZKY<sup>3</sup> HIROSHI NAKAJIMA<sup>41</sup>  
KAZUHIRO NAKAZAWA<sup>37</sup> JAN-UWE NESS<sup>42</sup> KUMIKO NOBUKAWA<sup>43</sup> MASAYOSHI NOBUKAWA<sup>44</sup> HIROFUMI NODA<sup>45</sup>  
HIROKAZU ODAKA<sup>33</sup> SHOJI OGAWA<sup>15</sup> ANNA OGORZALEK<sup>3,4,5</sup> TAKASHI OKAJIMA<sup>4</sup> NAOMI OTA<sup>46</sup> STEPHANE PALTANI<sup>1</sup>  
ROBERT PETRE<sup>4</sup> PAUL PLUCINSKY<sup>9</sup> FREDERICK S. PORTER<sup>4</sup> KATJA POTTSCHMIDT<sup>8,4,5</sup> KOSUKE SATO<sup>47</sup> TOSHIKI SATO<sup>48</sup>  
MAKOTO SAWADA<sup>29</sup> HIROMI SETA<sup>18</sup> MEGUMI SHIDATSU<sup>2</sup> AURORA SIMIONESCU<sup>12</sup> RANDALL SMITH<sup>9</sup> HIROMASA SUZUKI<sup>15</sup>  
ANDREW SZYMKOWIAK<sup>49</sup> HIROMITSU TAKAHASHI<sup>19</sup> MAI TAKEO<sup>28</sup> TORU TAMAGAWA<sup>25</sup> KEISUKE TAMURA<sup>8,4,5</sup>  
TAKAAKI TANAKA<sup>50</sup> ATSUSHI TANIMOTO<sup>51</sup> MAKOTO TASHIRO<sup>28,15</sup> YUKIKATSU TERADA<sup>28,15</sup> YUICHI TERASHIMA<sup>2</sup>  
YOHKO TSUBOI<sup>52</sup> MASAHIRO TSUJIMOTO<sup>15</sup> HIROSHI TSUNEMI<sup>33</sup> TAKESHI TSURU<sup>17</sup> AYŞEGÜL TÜMER<sup>8,4,5</sup>  
HIROYUKI UCHIDA<sup>17</sup> NAGOMI UCHIDA<sup>15</sup> YUUSUKE UCHIDA<sup>31</sup> HIDEKI UCHIYAMA<sup>53</sup> SHUTARO UEDA<sup>54</sup> YOSHIHIRO UEDA<sup>55</sup>  
SHINICHIRO UNO<sup>56</sup> JACCO VINK<sup>57,12</sup> SHIN WATANABE<sup>15</sup> BRIAN J. WILLIAMS<sup>4</sup> SATOSHI YAMADA<sup>25</sup> SHINYA YAMADA<sup>29</sup>  
HIROYA YAMAGUCHI<sup>15</sup> KAZUTAKA YAMAOKA<sup>37</sup> NORIKO YAMASAKI<sup>15</sup> MAKOTO YAMAUCHI<sup>24</sup> SHIGEO YAMAUCHI<sup>58</sup>  
TAHIR YAQOUB<sup>8,4,5</sup> TOMOKAGE YONEYAMA<sup>52</sup> TESSEI YOSHIDA<sup>15</sup> MIHOKO YUKITA<sup>59,4</sup> IRINA ZHURAVLEVA<sup>60</sup>  
ANDREW FABIAN<sup>61</sup> DYLAN NELSON<sup>62</sup> NOBUHIRO OKABE<sup>63</sup> ANNALISA PILLEPICH<sup>64</sup> CICELY POTTER<sup>65</sup> MANON REGAMEY<sup>66</sup>  
KOSEI SAKAI<sup>37</sup> MONA SHISHIDO<sup>31</sup> NHUT TRUONG<sup>8,4,5</sup> DANIEL R. WIK<sup>65</sup> JOHN ZUHONE<sup>9</sup>

<sup>1</sup>Department of Astronomy, University of Geneva, Versoix CH-1290, Switzerland

<sup>2</sup>Department of Physics, Ehime University, Ehime 790-8577, Japan

<sup>3</sup>Department of Astronomy, University of Maryland, College Park, MD 20742, USA

<sup>4</sup>NASA / Goddard Space Flight Center, Greenbelt, MD 20771, USA

<sup>5</sup>Center for Research and Exploration in Space Science and Technology, NASA / GSFC (CRESSST II), Greenbelt, MD 20771, USA

<sup>6</sup>Department of Physics, University of Tokyo, Tokyo 113-0033, Japan

<sup>7</sup>Department of Physics, Technion, Technion City, Haifa 3200003, Israel

<sup>8</sup>Center for Space Sciences and Technology, University of Maryland, Baltimore County (UMBC), Baltimore, MD, 21250 USA

<sup>9</sup>Center for Astrophysics | Harvard-Smithsonian, Cambridge, MA 02138, USA

<sup>10</sup>Lawrence Livermore National Laboratory, Livermore, CA 94550, USA

<sup>11</sup>Department of Astronomy, University of Michigan, Ann Arbor, MI 48109, USA

<sup>12</sup>SRON Netherlands Institute for Space Research, Leiden, The Netherlands

<sup>13</sup>ESO, Karl-Schwarzschild-Strasse 2, 85748, Garching bei München, Germany

<sup>14</sup>Centre for Extragalactic Astronomy, Department of Physics, University of Durham, Durham DH1 3LE, UK

<sup>15</sup>Institute of Space and Astronautical Science (ISAS), Japan Aerospace Exploration Agency (JAXA), Kanagawa 252-5210, Japan

<sup>16</sup>Department of Economics, Kumamoto Gakuen University, Kumamoto 862-8680 Japan

<sup>17</sup>Department of Physics, Kyoto University, Kyoto 606-8502, Japan

<sup>18</sup>Department of Physics, Tokyo Metropolitan University, Tokyo 192-0397, Japan

<sup>19</sup>Department of Physics, Hiroshima University, Hiroshima 739-8526, Japan

<sup>20</sup>Department of Physics, Fujita Health University, Aichi 470-1192, Japan

<sup>21</sup>Department of Astronomy and Physics, Saint Mary's University, Nova Scotia B3H 3C3, Canada

<sup>22</sup>California Institute of Technology, Pasadena, CA 91125, USA

<sup>23</sup>European Space Agency (ESA), European Space Research and Technology Centre (ESTEC), 2200 AG Noordwijk, The Netherlands

<sup>24</sup>Faculty of Engineering, University of Miyazaki, 1-1 Gakuen-Kibanadai-Nishi, Miyazaki, Miyazaki 889-2192, Japan

<sup>25</sup>RIKEN Nishina Center, Saitama 351-0198, Japan

<sup>26</sup>Leiden Observatory, University of Leiden, P.O. Box 9513, NL-2300 RA, Leiden, The Netherlands

<sup>27</sup>Kavli Institute for Astrophysics and Space Research, Massachusetts Institute of Technology, MA 02139, USA

<sup>28</sup>Department of Physics, Saitama University, Saitama 338-8570, Japan

<sup>29</sup>Department of Physics, Rikkyo University, Tokyo 171-8501, Japan

<sup>30</sup>Faculty of Physics, Tokyo University of Science, Tokyo 162-8601, Japan

<sup>31</sup>Faculty of Science and Technology, Tokyo University of Science, Chiba 278-8510, Japan

<sup>32</sup>*Department of Electronic Information Systems, Shibaura Institute of Technology, Saitama 337-8570, Japan*

<sup>33</sup>*Department of Earth and Space Science, Osaka University, Osaka 560-0043, Japan*

<sup>34</sup>*Department of Physics, University of Wisconsin, WI 53706, USA*

<sup>35</sup>*Department of Physics & Astronomy, Waterloo Centre for Astrophysics, University of Waterloo, Ontario N2L 3G1, Canada*

<sup>36</sup>*Institut de Recherche en Astrophysique et Planétologie (IRAP), Toulouse, France*

<sup>37</sup>*Department of Physics, Nagoya University, Aichi 464-8602, Japan*

<sup>38</sup>*Science Research Education Unit, University of Teacher Education Fukuoka, Fukuoka 811-4192, Japan*

<sup>39</sup>*Hiroshima Astrophysical Science Center, Hiroshima University, Hiroshima 739-8526, Japan*

<sup>40</sup>*Department of Data Science, Tohoku Gakuin University, Miyagi 984-8588*

<sup>41</sup>*College of Science and Engineering, Kanto Gakuin University, Kanagawa 236-8501, Japan*

<sup>42</sup>*European Space Agency(ESA), European Space Astronomy Centre (ESAC), E-28692 Madrid, Spain*

<sup>43</sup>*Department of Science, Faculty of Science and Engineering, KINDAI University, Osaka 577-8502, Japan*

<sup>44</sup>*Department of Teacher Training and School Education, Nara University of Education, Nara 630-8528, Japan*

<sup>45</sup>*Astronomical Institute, Tohoku University, Miyagi 980-8578, Japan*

<sup>46</sup>*Department of Physics, Nara Women's University, Nara 630-8506, Japan*

<sup>47</sup>*International Center for Quantum-field Measurement Systems (KEK/QUP), Tsukuba, Ibaraki 300-3256, Japan*

<sup>48</sup>*School of Science and Technology, Meiji University, Kanagawa, 214-8571, Japan*

<sup>49</sup>*Yale Center for Astronomy and Astrophysics, Yale University, CT 06520-8121, USA*

<sup>50</sup>*Department of Physics, Konan University, Hyogo 658-8501, Japan*

<sup>51</sup>*Graduate School of Science and Engineering, Kagoshima University, Kagoshima, 890-8580, Japan*

<sup>52</sup>*Department of Physics, Chuo University, Tokyo 112-8551, Japan*

<sup>53</sup>*Faculty of Education, Shizuoka University, Shizuoka 422-8529, Japan*

<sup>54</sup>*Kanazawa University, Kanazawa, 920-1192 Japan*

<sup>55</sup>*Department of Astronomy, Kyoto University, Kyoto 606-8502, Japan*

<sup>56</sup>*Nihon Fukushi University, Shizuoka 422-8529, Japan*

<sup>57</sup>*Anton Pannekoek Institute, the University of Amsterdam, Postbus 942491090 GE Amsterdam, The Netherlands*

<sup>58</sup>*Department of Physics, Faculty of Science, Nara Women's University, Nara 630-8506, Japan*

<sup>59</sup>*Johns Hopkins University, MD 21218, USA*

<sup>60</sup>*Department of Astronomy and Astrophysics, University of Chicago, Chicago, IL 60637, USA*

<sup>61</sup>*Institute of Astronomy, Cambridge CB3 0HA, UK*

<sup>62</sup>*Heidelberg University, Heidelberg, Germany*

<sup>63</sup>*Hiroshima University, Hiroshima 739-8526, Japan*

<sup>64</sup>*Max-Planck-Institut für Astronomie, Heidelberg, Germany*

<sup>65</sup>*University of Utah, Salt Lake City, UT 84112, USA*

<sup>66</sup>*University of Geneva, Geneva, Switzerland*